PCCP

Accepted Manuscript

ROYAL SOCIETY OF CHEMISTRY

www.rsc.org/pccp

Physical Chemistry Chemical Physics
CREATED USING THE RSC LaTeX PCCP ARTICLE TEMPLATE – SEE www.rsc.org/electronicfiles FOR DETAILS
ARTICLE TYPE www. rsc.org/xxxxxx | XXXXXXXX

Quantum dynamical investigation of the isotope effect in H_2 formation on graphite at cold collision energies

Marta Pasquini,[a] Matteo Bonfanti,[a] and Rocco Martinazzo[a,b,*]

Received Xth XXXXXXXXXX 20XX, Accepted Xth XXXXXXXXX 20XX
First published on the web Xth XXXXXXXXXX 200X
DOI: 10.1039/b000000x

Eley-Rideal abstraction of hydrogen atoms on graphitic surfaces at cold collision energies was investigated with a time-dependent wave packet method within the rigid-flat surface approximation, with a focus on hydrogen-deuterium isotopic substitutions. It is found that the marked isotope effect of collinear collisions disappears when the full dimensionality of the problem is taken into account, thereby suggesting that abstraction is less direct than commonly believed and proceeds through glancing rather than head-on collisions. On the contrary, a clear isotope effect is observed for "hot-atom" formation, which appears to be strongly favored for heavy projectiles because of their higher density of physisorbed states. Overall, the dynamics is essentially classical and reasonably well described by quasi-classical trajectory methods at all but the lowest energies ($\lesssim$10 meV). Comparison of the results obtained in the (substrate) adiabatic and diabatic limits suggests that the reaction is only marginally affected by the lattice dynamics, but highlights the importance of including energy dissipation processes in order to accurately describe the internal excitation of the product molecules.

1 Introduction

In recent years, hydrogen recombination on graphitic surfaces has been the subject of many theoretical investigations, largely motivated by the primary role that this process plays in the chemistry of the interstellar medium (ISM), the extremely cold and rarefied gas which fills the space between stars. H_2 is in fact the most abundant molecular species in many interstellar environments, it takes part in most of the reactions forming complex molecular species and it is the principal cooling agent during the gravitational collapse of the clouds that eventually leads to star formation[1]. Efficient formation pathways for H_2 are needed to explain its abundance since hydrogen molecules are continuously dissociated by the intense stellar UV radiation field and cosmic rays. It is now widely accepted that hydrogen formation has to occur on the surface of the interstellar dust grains[2–4]. The latter are typically μm-sized and contain a silicate core covered by an "organic refractory" mantle, though the tiniest particles are entirely carbonaceous and most likely are simple polycyclic aromatic hydrocarbon (PAH) molecules[5]. Hence, in all but the coldest (so-called molecular) clouds where H_2O and CO_2 ice mantles cover the silicate core, the surface where hydrogen recombination occurs is mainly carbonaceous, and this makes hydrogen-graphite a prototypical system for studying hydrogen formation in space[6–21].

In general, a reaction at the gas-surface interface may occur through three different mechanisms. In the Langmuir-Hinshelwood (LH) mechanism, both reactants adsorb on the surface, thermalize with it and diffuse until they encounter each other and react. In the Eley-Rideal (ER) mechanism, on the other hand, only one of the reagents is adsorbed on the surface, the second comes from the gas phase and forms the molecule in a direct collision process. A third, intermediate ("hot-atom", HA) mechanism is possible, particularly when light atoms are involved: one of the two reactants is trapped on the surface but it is not equilibrated, rather hyperthermally diffuses until it finds its reaction partner. In the case of hydrogen recombination on graphite, the reaction mechanism strongly depends on the physical conditions, and several scenarios are possible, depending whether physisorbed or chemisorbed species are involved.

Hydrogen atoms may be adsorbed on the regular (0001) surface of graphite in the shallow ($\sim$40 meV deep) physisorption well[22] and diffuse quickly even in the zero temperature limit thanks to efficient tunneling through the tiny (5 meV high) barrier between neighboring adsorption sites[23]. Hydrogen recombination follows physisorption of a H atom[24], and may occur through LH/HA[25,26] or ER[19,27] reactions. In this case, physisorption is facile - though rather inefficient[24] - but desorption from the shallow well is a limiting factor, since refreshment of the surface is complete at a very small (surface) temperature, $T_s \sim$ 30-40 K.

Hydrogen atoms may also chemically adsorb on the

[a] *Universitá degli Studi di Milano, Dipartimento di Chimica, via Golgi 19, 20133 Milano, Italy.*
[b] *Consiglio Nazionale delle Ricerche, Istituto di Scienze e Tecnologie Molecolari, Milano, Italy.*

graphitic surface, and form a strong (covalent) bond with one of the substrate atoms, a process that has been extensively studied, both experimentally[28–30] and theoretically[31,32]. In this case, the binding carbon atom moves out of the surface plane by about 0.4 Å as a consequence of the $sp^2 \rightarrow sp^3$ rehybridization of its valence orbitals, "puckers" the surface and store considerable energy ($\sim$0.8 eV) which may released to the lattice upon hydrogen abstraction. Importantly, a $\sim$0.20 eV barrier to chemisorption appears which prevents sticking of cold hydrogen atoms, as observed experimentally using cold atom beams[33], and recently confirmed theoretically by converged quantum scattering simulations of the sticking dynamics[34,35]. Diffusion of chemisorbed H atoms is prevented by a large barrier that matches the desorption threshold - *i.e.* H atoms prefer to desorb rather than diffuse - thereby ruling out the possibility of a LH recombination. Hence, in this chemisorbed regime hydrogen species which manage to stick are stable on the surface up to high temperatures (T_s $\sim$400-500 K) and form H_2 molecules either through an ER or a HA reaction mechanism.

In this article we focus on the Eley-Rideal recombination involving chemisorbed H species. The reaction is strongly exothermic and barrierless, and thus proceeds down to very low collision energies[33,36], forming vibrationally hot product molecules[37,38]. It was thoroughly scrutinized theoretically on several aspects[6–21] - namely, the rovibrational distribution of the products, the presence of steering effects in the dynamics, the dynamical role of the binding carbon atom, the effect of surface temperature, the competition with non-activated sticking to neighboring carbon atoms and the influence of non-zero surface coverage on the reaction - but only occasionally considered for the isotope effect[39,40]. Here we reconsider this issue by focusing on the cold collision energy regime which is relevant for the chemistry of the interstellar clouds. We do this by employing a time-dependent wavepacket method within the sucessful rigid, flat-surface approximation[41,42] that was already applied in the past to the present reaction system[11,18–20,27]. The specific implementation that allows us to address collisions at such cold collision energies (down to $\sim 10^{-4}$ eV $\approx$ 1.2 K), - already applied to the H+H isotopic combination[19] - makes use of two independent wavepacket propagations that, exploiting the linearity of the Schrödinger equation, remove the limitations of a standard, one-wavepacket propagation[43]. The strategy is rather general for quantum simulations in the time domain, and is being used in larger dimensional quantum dynamical studies of the title process which include the motion of surface atoms and, thus, energy dissipation to the surface.

The paper is organized as follows. Section 2 describes in detail our two-wavepacket method, Section 3 focuses on some methodological aspects specific of the Eley-Rideal reombination problem, Section 4 describes the results obtained for the four isotopic combinations considered, and Section 5 summarizes and concludes.

2 Time-energy mapping at cold collision energies

One of the main advantages of time-dependent wave packet methods over time-independent ones is that with a single propagation one obtains energy resolved information for a given initial internal state and a range of collision energies. This is accomplished with the help of a time-energy mapping of the dynamics which is made possible by enforcing two 'asymptotic' conditions on the initial wave packet: the wavepacket is chosen to be (i) localized in the asymptotic region of the reagents and (ii) with *incoming* momentum components only (*i.e.* momentum components towards the interaction region, $p < 0$). These conditions thus mimic the *classical* approach to a collision problem, where trajectories are started in the asymptotic region of the reagents with momentum vectors directed towards each other. They challenge the applicability of the time-dependent method to the cold collision energy regime since they severely limit the width Δp of the initial momentum wavefunction ($\Delta p \lesssim p_0$, if $-p_0$ is the average initial momentum), hence the minimum width Δx of the initial wavepacket ($\Delta x \gtrsim \hbar/\Delta p \gtrsim \hbar/p_0$). This is clearly unpleasant if one is interested in covering a large range of collision energies with a single calculation and, in addition, wants to keep the grid dimensions reasonably small.

In order to make progress let us recall why the conditions above are crucial for the standard time-energy mapping. Firstly, they relate the forward propagation to the (differential) eigenprojector on the energy shell $\delta(E-H)$, namely through

$$\begin{aligned}\int_0^\infty e^{iEt}\,\langle \mathbf{x}\,|\,\Psi_t\rangle\,dt &\approx \int_{-\infty}^{\infty} e^{iEt}\,\langle \mathbf{x}\,|\,\Psi_t\rangle\,dt \\ &= 2\pi\,\langle \mathbf{x}\,|\,\delta(E-H)\,|\,\Psi_0\rangle\end{aligned}$$

Here $|\Psi_t\rangle = U_t\,|\Psi_0\rangle = e^{-iHt}\,|\Psi_0\rangle$ is the time-evolving wave packet (we use atomic units throughout, $\hbar = 1$) and $\mathbf{x}$ is an arbitrary point in the system configuration space which is *not* in the reagent region. This expression holds because assumptions (i) and (ii) guarantee that in this case the past dynamics makes no contributions to the amplitude to be integrated. Secondly, they relate the initial state $|\Psi_0\rangle$ to the desired scattering states through the appropriate energy weights. Indeed, if α is the initial internal state, the r.h.s. of the above equation simplifies to

$$\begin{aligned}2\pi\,\langle \mathbf{x}\,|\,\delta(E-H)\,|\,\Psi_0\rangle &= 2\pi \sum_\beta \langle \mathbf{x}|E\beta+\rangle\,\langle E\beta+|\Psi_0\rangle \\ &\approx 2\pi\,\langle \mathbf{x}|E\alpha+\rangle\,\langle E\alpha|\Psi_0\rangle\end{aligned}$$

Here $|E\beta+\rangle$ is a scattering (outgoing) eigenstate corresponding to the precollisional $|E\beta\rangle$ eigenstate, the sum runs over the open channels of every arrangement, and in the last step we have used

$$\begin{aligned}\langle E\beta+|\Psi_0\rangle &= \lim_{t\to-\infty}\langle E\beta|U_t^{0,\beta\,\dagger}U_t|\Psi_0\rangle \\ &= \delta_{\alpha\beta}\,\langle E\alpha|\Psi_0\rangle\end{aligned}$$

($U_t^{0,\beta}$ being the free-evolution operator for channel β) which holds thanks to the conditions above. Finally, one obtains

$$\langle \mathbf{x}|E\alpha+\rangle = \frac{1}{2\pi}\frac{\sqrt{\bar{v}}}{\psi_0(-\bar{p})}\int_0^\infty e^{iEt}\,\langle \mathbf{x}\,|\,\Psi_t\rangle\,dt \qquad (1)$$

where $\langle E\alpha|\Psi_0\rangle$ has been expressed in terms of the initial momentum wavefunction $\psi_0(p)$ for the motion in the scattering coordinate - *i.e.* $\langle E\alpha|\Psi_0\rangle \equiv \psi_0(-\bar{p})/\sqrt{\bar{v}}$ - and $\bar{p}$, $\bar{v}$ (≥ 0) are the entrance channel momentum and speed, respectively.

With this premise in mind, let us now show how to exploit the linearity of the Schrödinger equation and obviate condition (ii) by (independently) propagating two wavepackets in place of one[43]. If $\psi_a(p)$ is a generic (momentum) wavefunction for the motion in the entrance-channel scattering coordinate (to be used in $|\Psi_a\rangle = |\psi_a\alpha\rangle$ as initial state) we may write, under the sole condition (i) above,

$$\begin{aligned}&2\pi\,\langle \mathbf{x}\,|\,\delta(E-H)\,|\,\Psi_a\rangle = \\ &\frac{2\pi}{\sqrt{\bar{v}}}\left\{\langle \mathbf{x}|E\alpha+\rangle\,\psi_a(-\bar{p}) - \sum_\beta S^*_{\alpha\beta}(E)\,\langle \mathbf{x}|E\beta+\rangle\,\psi_a(\bar{p})\right\}\end{aligned}$$

where $S_{\alpha\beta}(E)$ is the $\beta\to\alpha$ S-matrix element at energy E and the sum runs over the open channels of the reagent arrangement only. The above formula holds for any point $\mathbf{x}$ and can be obtained by noticing that $|\Psi_a\rangle$ localizes in the asymptotic region, since this allows one to use the *asymptotic* expansion of scattering eigenstates contained in the energy-shell projector, $\delta(E-H) = \sum_\beta |E\beta+\rangle\langle E\beta+|$. The second term on the r.h.s. of the above expression represents the contribution of the *outgoing* components to the energy shell, *i.e.* the collision processes $\beta\to\alpha$ which do have *outgoing* components in channel α and necessarily overlap with those contained in $|\Psi_a\rangle$. This term disappears, of course, in the traditional approach when condition (ii) is enforced. Now, using two (linearly independent) initial states ($a = 1,2$) the above equation reduces to a 2×2 linear system in the variables $X = \langle \mathbf{x}|E\alpha+\rangle$ and $Y = \sum_\beta S^*_{\alpha\beta}(E)\,\langle \mathbf{x}|E\beta+\rangle$ which can be easily solved to give

$$\begin{aligned}\langle \mathbf{x}|E\alpha+\rangle = &\frac{\sqrt{\bar{v}}}{\psi_1(-\bar{p})\psi_2(\bar{p}) - \psi_1(\bar{p})\psi_2(-\bar{p})}\times \\ &[\psi_2(\bar{p})\,\langle \mathbf{x}\,|\,\delta(E-H)\,|\,\Psi_1\rangle - \psi_1(\bar{p})\,\langle \mathbf{x}\,|\,\delta(E-H)\,|\,\Psi_2\rangle]\end{aligned}$$

This is the desired expression that we were looking for and that can be further re-expressed in terms of time-evolving wavepackets

$$2\pi\,\langle \mathbf{x}\,|\,\delta(E-H)\,|\,\Psi_a\rangle = \int_{-\infty}^{\infty} e^{iEt}\,\langle \mathbf{x}\,|\,\Psi_{a,t}\rangle\,dt$$

using, in general, both the forward and the backward evolutions. The resulting equation generalizes Eq. (1) *without* the requirement of condition (ii). It is easy to check that when enforcing this additional condition one wavepacket is sufficient to get the desired scattering eigenstate, and that the above expression does indeed reduce to Eq. (1) (just use $\psi_1(\bar{p})\sim 0$ and consider $\mathbf{x}$ in the product region so that only the $t>0$ evolution is required).

Finally, it is advantageous in practice to further simplify the expression above by employing time-reversal invariant initial states, *i.e.* states for which $T\,|\Psi_a\rangle = |\Psi_a\rangle$ holds, T being the antiunitary time-reversal operator. Indeed, in this case,

$$\langle \mathbf{x}\,|\,U_t\Psi_a\rangle = \langle \mathbf{x}\,|\,U_tT\Psi_a\rangle = \langle \mathbf{x}\,|\,TU_{-t}\Psi_a\rangle = \langle \mathbf{x}\,|\,U_{-t}\Psi_a\rangle^*$$

holds provided $[T,H]=0$, and the final working equation becomes

$$\begin{aligned}\langle \mathbf{x}|E\alpha+\rangle = &\frac{1}{2\pi}\frac{\sqrt{\bar{v}}}{i\Im(\psi_1^*(\bar{p})\psi_2(\bar{p}))} \\ &\left\{\psi_2(\bar{p})\Re\int_0^\infty e^{iEt}\,\langle \mathbf{x}\,|\,\Psi_{1,t}\rangle\,dt\right. \\ &\left. -\,\psi_1(\bar{p})\Re\int_0^\infty e^{iEt}\,\langle \mathbf{x}\,|\,\Psi_{2,t}\rangle\,dt\right\}\end{aligned}$$

thereby involving only the forward evolution. Here, we can choose wavepackets for the translational motion that are 'even' or 'odd' with respect to a reflection on a plane passing through their average position x_0, whose corresponding momentum wavefunctions are given by $\psi_1(p) = \phi_g(p)e^{-ipx_0}$ and $\psi_2(p) = -i\phi_u(p)e^{-ipx_0}$, where $\phi_g(\phi_u)$ is a *real* even (odd) function of p. This reduces the scattering amplitude to

$$\begin{aligned}\langle \mathbf{x}|E\alpha+\rangle = &\frac{1}{2\pi}\sqrt{\bar{v}}e^{-i\bar{p}x_0} \\ &\left\{\frac{1}{\phi_g(\bar{p})}\Re\int_0^\infty e^{iEt}\,\langle \mathbf{x}\,|\,\Psi_{g,t}\rangle\,dt\right. \\ &\left. -\,\frac{i}{\phi_u(\bar{p})}\Re\int_0^\infty e^{iEt}\,\langle \mathbf{x}\,|\,\Psi_{u,t}\rangle\,dt\right\}\end{aligned} \qquad (2)$$

in which the distinct real/imaginary contributions come from the initially "even"/"odd" time-evolving wavepackets (apart from the irrelevant phase factor $e^{-i\bar{p}x_0}$). This means that the two can be computed and managed independently of each other and stored as independent parts of a single complex array.

In this work we have used Eq. (2) in place of Eq. (1) in order to perform the time-energy mappings needed to extract energy resolved information from the time propagations. Thus, for example, the probability $P_{\alpha\to\beta}$ for the collisional transition to a product internal state β reads as usual *

$$P_{\alpha\to\beta}(E) = 2\pi \langle E\alpha + | F_\beta^\infty | E\alpha + \rangle = \frac{2\pi}{m'} \Im \left\{ \Phi^*_{\alpha\to\beta}(R_\infty, E) \frac{\partial \Phi_{\alpha\to\beta}}{\partial R}(R_\infty, E) \right\}$$

where F_β^∞ is the flux operator in the β product channel†, m' is the product reduced mass and $\Phi_{\alpha\to\beta}(R,E) = \langle R, \beta | E\alpha + \rangle$ has to be known for a large distance R_∞ in the product arrangement. The only difference with the standard approach is that now $\Phi_{\alpha\to\beta}$ is obtained from the amplitude of Eq. (2) rather than from Eq. (1).

For completeness Table 1 summarizes the main formulas used in the standard approach (with the common choice of a Gaussian wavepacket as initial translational state) and in this work. Notice that the 'even' and 'odd' components in our approach correspond to the ground and the first excited state of a harmonic oscillator potential centered in x_0; the choice $\delta' = \sqrt{3}\delta$ for the width appearing in ψ_u guarantees that the two wavefunctions have the same spread Δp in momentum space.

3 Dynamical model and methodology

To simulate the Eley-Rideal process, we considered a projectile atom of mass m_P and position $\mathbf{x}_P$ which scatters off a chemisorbed target atom of mass m_T and position $\mathbf{x}_T$. In line with our previous work[17–20,27] a reduction of the number of relevant coordinates is achieved by invoking the rigid, flat surface approximation[41,42] that makes $\mathbf{P}_\parallel$ (the total momentum parallel to the surface) and $J_\mathbf{n}$ (the projection of the total angular momentum on the surface normal) conserved quantities ‡. In this simplified 3D description, the phonons of the graphitic surface are neglected and the interaction of the target/incident atoms with the surface is site-independent. On the other hand, the (important) role of the carbon binding the target can be included in the potential energy surface (PES) governing the dynamics in two opposite dynamical limits[11]. In the (substrate) *diabatic* limit the reaction dynamics is supposed to be so fast that the C atom remains frozen in its puckered configuration, whereas in the *adiabatic* limit the substrate atom relaxes istantaneously during the (supposedly slow) recombination process. These limits give rise to two different PESs with rather different exothermicity (3.90 eV in the adiabatic potential and 3.03 eV in the diabatic one), on account of the energy left on the lattice in the diabatic model. Apart from this, though, the energy landscape is rather similar in the two dynamical limits, and displays a downhill (barrierless) route to the molecular product[11].

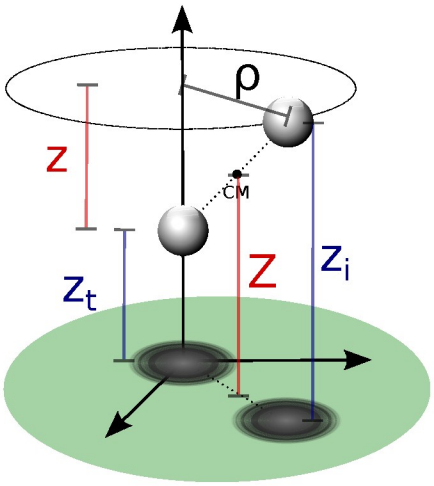

Fig. 1 Schematic representation of the coordinates adopted for the rigid, flat-surface modeling of the ER recombination dynamics. In blue, the reagent coordinates z_P and z_T, and in red the product coordinates Z and z. In both cases, ρ describes the motion parallel to the surface.

In modeling the dynamics, the relevant dynamical variables are conveniently chosen to be either the height of the two atoms above the surface (z_P, z_T for the projectile and target atoms, respectively) and their separation on the surface plane (ρ), or the center of mass height $Z = (m_P z_P + m_T z_T)/(m_P + m_T)$, the relative height $z = z_P - z_T$ and ρ (see Fig. 1). The first is a "reagent" set of coordinates which best suits to compute energy resolved (in)elastic scattering, atom exchange and trapping probabilities, the second is a "product" set which is ideal for determining the rovibrational populations of the reaction products.

As for the wavepacket propagation, a detailed description of our strategy, which stems from previous work by Lemoine and Jackson[42], has been presented elsewhere[18]. Briefly, for the cartesian coordinates (either (z_T, z_P) or (Z, z)) the wavepacket is represented on a uniform grid, and the pseudospectral strategy involving the use of Fast Fourier Transforms (FFTs) is exploited to move efficiently back and forth between coordinate and momentum space. For the cylindrical coordinate, the discrete Bessel transform (DBT) of Lemoine[44] is used instead,

∗ See, for example, the Appendix in Ref. 18 for a time-dependent perspective.

† The flux operator appearing here, F_β^∞, is defined as the Heisenberg derivative of the projector onto the products internal state β, $F_\beta^\infty = i[H, P_\beta^\infty]$. The latter reads as $P_\beta^\infty = h_\infty(R) |\beta\rangle \langle\beta|$ where R is the product scattering coordinate (operator), $h_\infty(x) = \{1$ for $x > R_\infty, 0$ otherwise$\}$ is the usual Heaviside function centered on a large distance R_∞ and β labels the relevant product internal state.

‡ Conservation of the angular momentum gives rise to a partial wave expansion. At normal incidence (the case considered in this work) only the zero angular momentum partial wave is required.

	1WP	2WP
initial translational state(s)	$\psi_0(x) = (\frac{1}{2\pi\delta^2})^{1/4} e^{-(x-x_0)^2/4\delta^2} e^{-ip_0(x-x_0)}$	$\psi_g(x) = (\frac{1}{2\pi\delta^2})^{1/4} e^{-(x-x_0)^2/4\delta^2}$ $\psi_u(x) = (\frac{1}{6\pi\delta^2})^{1/4} e^{-(x-x_0)^2/12\delta^2} (x-x_0)/\sqrt{3}\delta$
energy weights	$g(E) = \sqrt{8\pi}\frac{mm'\delta}{p} e^{-2\delta^2(p-p_0)^2}$	$g(E) = 2^{5/2} 3^{3/4} \sqrt{\pi}\delta^2 mm' e^{-4\delta^2 p}$
reduced amplitudes	$\phi_\beta^\infty(E) = \int_0^\infty e^{iEt} \langle R_\infty \beta \vert \Psi_t \rangle dt$	$\phi_\beta^\infty(E) = \Re \int_0^\infty e^{iEt} \langle R_\infty \beta \vert \Psi_{g,t} \rangle dt +$ $-i\Re \int_0^\infty e^{iEt} \langle R_\infty \beta \vert \Psi_{u,t} \rangle dt$

Table 1 Comparison between the traditional wavepacket approach for initial-state selected dynamics (1WP) and the one (2WP) adopted in this work. The momentum p is related to the total energy E through $p = \sqrt{2m(E-\varepsilon_\alpha)}$, where ε_α is the channel energy in the pre-collisional state, and the reaction probabilities are obtained from $P_\beta = \Im\left(\phi_\beta^\infty D_R \phi_\beta^\infty\right)/g(E)$. Here, $D_R\phi_\beta^\infty$ is analogous to ϕ_β^∞, and involves the derivate with respect to the scattering coordinate R evaluated at the large value R^∞. In the table entries m and m' are the reduced masses in the reagent and product arrangement, respectively, δ is the width of the initial wavepacket in the scattering coordinate and x_0 (p_0) the average position (momentum).

since Bessel functions correctly handle the boundary conditions in the cylindrical radial coordinate and guarantee a numerically stable representation of the kinetic energy operator. The length of the grid along ρ (which sets the maximum value of the classical impact parameter) was set to 13 Å irrespective of the isotopic combination, after carefully testing that this value gives reasonably well converged cross sections. The number of grid points, on the other hand, was chosen differently for each reaction in order to guarantee a common value of the maximum momentum on the ρ axis. The same consideration guided the choice for the grid spacing of the cartesian coordinates, for which an energy cutoff of ~ 5.5 eV was introduced. Time propagation was performed with the split-operator method[45], using multithreaded routines for FFTs and linear algebra operations which are available in commercial packages.

The initial wavepackets were built as a product of three terms, namely (i) a wavepacket centered in the reagent asymptotic region and describing the motion of the incident atom normal to the surface ($\psi_a(z_P)$), (ii) a vibrational wave function for the target atom bound to the surface ($\phi_v(z_T)$) and (iii) a *quasi*-plane wave for the relative motion parallel to the surface ($\phi_\parallel(\rho)$). We choose to consider only the vibrational ground state of the target atom ($v = 0$), since it is the only one relevant for the ISM chemistry, the excitation energy to v=1 being already too large for the typical diffuse clouds conditions. The translational component of the initial wavefunctions (two for each calculation) was 0.2 Å large in coordinate space and zero-centered in momentum space, in accordance with the methodology introduced in Section 2 (see Table 1). As for the motion along ρ, since we considered normal incidence only we picked up the lowest-momentum Bessel function supported by the adopted grid, *i.e.* a *quasi*-uniform initial state.

Practical application of the two-wavepacket strategy requires the use of a sufficiently large grid to accommodate both the longest wavelength of interest and a reasonably good absorbing potential. In practice, this is needed in the entrance arrangement only since product (open) channels benefit of the reaction exothermicity leading ultimately to short-wavelength outgoing components at all but the threshold energies. Following our previous experience, we adopted Manolopoulos' transmission-free absorbing potentials[46] (APs). These were originally designed to completely remove transmission at high energy - provided the appropriate boundary conditions are enforced by the adopted discretization -, thereby allowing one to deal only with the low-energy reflection problem. These APs have one parameter only, the strength E_{min} of the potential, which sets both the energy scale (the lowest kinetic energy with a reflection probability less than 1%) and the AP length $\lambda_{max} = h/\sqrt{2mE_{min}}$. In the typical applications we are interested in, *i.e.* hydrogen atoms at $10^{-3} - 10^{-4}$ eV, an absorption length of ~ 30 Å is required, *i.e.* a rather smooth AP which is slowly absorbing. As a consequence, propagation requires rather long times[19] (75-100 ps), which are anyhow necessary to obtain energy resolved results at low energies.

Probabilities were computed with the flux analysis outlined in Section 2. In particular, total Eley-Rideal cross sections

	H + H/C	H + D/C	D + H/C	D + D/C
t_{tot} / ps	100	100	100	100
Δt / fs	0.25	0.25	0.25	0.25
$z_P(0)$ / Å	15.0	15.0	15.0	15.0
n_P	675	675	960	960
Δz_P / Å	0.06	0.06	0.0426	0.0426
z_P-flux line / Å	16.0	16.0	16.0	16.0
z_P-E^{AP}_{min} / meV	0.14	0.14	0.06	0.06
n_T	125	180	125	180
Δz_T / Å	0.06	0.0426	0.06	0.0426
z_T-flux line / Å	5.0	5.0	5.0	5.0
z_T-E^{AP}_{min} / meV	14.2	6.1	14.2	6.1
n_ρ	150	170	170	210
ρ-flux line / Å	11.0	11.0	11.0	11.0
ρ-width / Å	13.0	13.0	13.0	13.0

Table 2 Parameters used in 3*D* calculations with the "reagent" set of coordinates. t_{tot} is the total propagation time, Δt the time step and $z_P(0)$ the (average) initial height of the projectile above the surface, Δz_P and Δz_T are the grid spacings and n_P, n_T and n_ρ the numbers of grid points. E^{AP}_{min} is the energy scale of the APs and the "flux line" parameters denote the starting positions of the APs, which are also the positions of the surfaces used for flux analysis.

were obtained from the flux through the appropriate surfaces in both product and reagent coordinates, whereas the rovibrational H_2 populations were conveniently determined in product coordinates. Cross sections for hot–atoms formation σ_{HA} were obtained from calculations in "reagents" coordinates, upon projecting the flux exiting along ρ onto the combined bound states of the incident and the target atoms. As a consequence, σ_{HA} describes formation of pairs of atoms freely moving on the surface with an energy higher than the desorption threshold but channeled in the relative motion *parallel* to the surface. Specifically, the energy of the relative motion along ρ is given by $E_\rho = E - \varepsilon^P_v - \varepsilon^T_{v'}$ where ε^P_v ($\varepsilon^T_{v'}$) is the energy of the bound state in the surface-projectile (target) potential in which the incidon (targon) is found. Realistic surfaces present corrugation, fluctuations and dissipative effects, which make these "hot-atoms" metastable only - they either relax to stable species or desorb from the surface - nevertheless, the computed σ_{HA} represent reasonable order-of-magnitude estimates of the hot-atom formation cross-sections.

Table 2, summarizes the main parameters adopted for the simulations in reagent coordinates. Parameters in product coordinates were chosen to guarantee a similar accuracy down to a reasonably small collision energy (∼meV); at lower energies, only the reagent set can accommodate the large APs necessary to obtain converged results [19].

We further performed quasi-classical trajectory (QCT) calculations to single out genuine quantum effects in the reaction dynamics. Target vibrational energy levels were obtained, as in the wave packet calculations, by standard diagonalization of the adsorbate-substrate Hamiltonian in the sinc-discrete variable representation (DVR), and used to sample target initial coordinate and momentum. The incident atom was placed at $z_P(0) = 8.0$ Å, and propagation carried out for sufficiently long times (up to 50 ps) to obtain converged results down to low collision energies (10^{-4} eV), running 100000 trajectories for each selected energy.

4 Results and discussion

In the following, we describe the results of the quantum calculations that we performed on both the adiabatic and the diabatic model developed by Sha *et al.* [11] to describe hydrogen recombination on graphite. We shall use "AonB" to indicate the process in which the A atom from the gas phase (the *incidon*) collides with the chemisorbed B atom (the *targon*):

$$A_{(g)} + B_{ad} \rightarrow AB_{(g)}$$

and consider the possible isotopic substitutions (A,B=H,D), with the target atom in its ground-vibrational state. We first describe the collinear 2D case where the incident atom collides on top the targon. This case shows a clear isotope effect, essentially classical in nature, that can be interpreted by means of a simple impulsive model of the dynamics. Next, we describe the more realistic 3D calculations, where the main constraints of the reduced-dimensional collinear dynamics are removed. In this case reliable reaction cross-sections can be computed, which can eventually be turned into rate constants useful for astrophysical modeling. As we shall see, the most striking feature of relaxing the above mentioned dynamical constraint (often invoked in qualitative descriptions of an Eley-Rideal reaction) is the disappearance of the isotope effect, a signature that the dynamics is less direct than commonly believed.

4.1 2D calculations

Fig. 2 reports the results for collinear reaction probabilities for the adiabatic potential, showing a clear isotope effect for each collision energy, though qualitatively different depending on the energy range considered. Similar results were obtained for the diabatic model (not shown).

At high collision energy ($E_{coll} \gtrsim 0.2$ eV) the behavior of the probability curves is rather classical and well captured by a simple, *quasi*-classical impulsive model of the dynamics*. In this model, the projectile with mass m_P and speed $v_P = \sqrt{2E_{coll}/m_P}$ undergoes a binary collision with the target

* We term it *quasi*-classical because it makes use of the quantum distribution of the precollisional targon momenta.

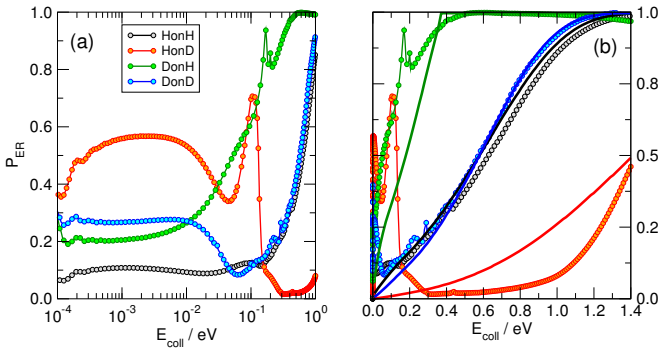

Fig. 2 ER recombination probabilities from 2D collinear calculations with the adiabatic model, as a function of the collision energy in both log (left panel) and linear (right panel) scale. In (b) the thick lines are the results of the *quasi*-classical impulsive model described in the main text, color coded as the quantum results.

of mass m_T and speed v_T, slows down its motion, and gets captured by the targon after the latter elastically bounces off the surface. Reaction occurs when the final kinetic energy of the targon $E_T^{'}$ is larger than E_R, a dynamical threshold which replaces the details of the dynamics and filters out those trajectories in which the targon is too slow to capture the projectile before leaving the reaction region (*i.e.* the surface).

The final kinetic energy $E_T^{'}$ is determined by the post-collisional target velocity $v_T^{'}$, as results, in turn, by the acceleration provided by the strong H-H interaction and by the above two sequential collisions, that is through the sequence

$$v_T = V - \frac{\mu}{m_T} v \overset{(i)}{\rightarrow} V - \frac{\mu}{m_T} \tilde{v} \overset{(ii)}{\rightarrow} V + \frac{\mu}{m_T} \tilde{v} \overset{(iii)}{\rightarrow} -V - \frac{\mu}{m_T} \tilde{v}$$

where (i) is the acceleration of the colliding pair, (ii) the projectile-targon collision and (iii) the bounce of the targon off the surface. Here $V = (m_P v_P + m_T v_T)/(m_P + m_T)$ is the center of mass speed of the colliding pair, $v = v_P - v_T$ is their initial relative velocity, $\tilde{v} = \sqrt{v^2 + 2D_m/\mu}$ (D_m being the H-H well depth) and $\mu = m_P m_T/(m_P + m_T)$ the reduced mass of the binary system. Hence, the reaction condition $E_T^f(v_T, v_P) > E_R$, determines a domain $\mathscr{V}(v_P)$ of target velocities leading to reaction, and the reaction probability P follows by integrating the distribution of target velocities $g(v)$ over $\mathscr{V}(v_P)$ for each value of the collision energy $E_{coll} = m_P v_P^2/2$.

It then remains to establish what is the most appropriate velocity distribution function $g(v)$ to be used. In the true impulsive limit $g(v)$ would simply be $g(v) = m_T |\phi_v(m_T v)|^2$ where $\phi_v(p)$ is the momentum space wavefunction of the target initial vibrational state ($v = 0$ in our case). However, this limit does not strictly hold in our case since the (high-frequency) target vibration ω_0 sets a bound to the collision time $\tau << \omega_0^{-1}$ which only attains at some eV of collision energy, as can be seen upon noticing that $\tau^2 \approx \frac{1}{2} m_T r_0^2/(E_{coll} + D_m)$, where r_0 is the potential range and $\omega_0^2 = 2\alpha^2 D_T/m_T$ (here, D_T is the targon-surface well depth and α^{-1} is the length scale of the Morse potential used to represent the targon-surface interaction, $\alpha^{-1} \approx r_0$). In other words, the targon atom performs one-two vibrations during the collision, and this makes the above mentioned vibrational distribution particularly inadequate for the lightest targets. To remedy this deficiency, and keep the model as simple as possible, we assume that the appropriate momentum distribution keeps the same shape and average but is bound to describe the increase of the average kinetic energy due to the interaction with the projectile, *i.e.* $\langle \Delta p^2 \rangle = \langle \Delta p_0^2 \rangle + 2 m_T D_{eff}$ where D_{eff} is an effective interaction energy and $\langle \Delta p_0^2 \rangle$ is the width of the bare momentum distribution of the target. This amounts to replace the original targon frequency ω_0 determining $\phi_v(p)$ with an effective frequency $\omega = \omega_0 + 4D_{eff}/\hbar$.

The results of such modeling for the adiabatic limit are given in Fig. 2 as full lines (panel (b)), color coded as the results of the quantum simulations. We set $E_T = 3.4$ eV, $D_m = 4.0$ eV, and $D_{eff} = 0.124$ eV to obtain a reasonable representation of the quantum results. Similar agreement was found for the diabatic model, using the same values of parameters except for D_{eff} which had to be increased to 0.250 eV, in accordance with the larger frequency of the H-graphite motion in the diabatic limit*.

The model is rather crude but, as can be seen from Fig. 2, it captures the main aspects of the dynamics and reproduces the isotope effect observed at high energies. The increase of the reaction probability with increasing m_P/m_T is a consequence of the larger range of targon initial velocities leading to sufficiently fast post-collisional targon atoms. Thus, in this classical energy regime, the largest isotope effect (*i.e.* the largest overall difference in reactivitiy) occurs at the "threshold" energy of the $m_P/m_T = 1$ case, ~ 0.6 eV in Fig. 2. This is the prototypical case where the projectile atom completely transfers its energy *when the targon is at rest* ($v_T = 0$), and thus represents a sort of transition between two different dynamical behaviours.

At low energies ($E_{coll} \lesssim 0.2$ eV), on the other hand, the dynamical outcome is largely determined by the details of the interaction potential, and by the quantum character of the dynamics that becomes more and more marked the smaller the energy is. As a consequence, for instance, the HonD combination (barely reactive at high energies) becomes more reactive at low energies than the "references", equal-mass combinations HoH and DonD. Thus, apart from the complicated details of the curves that appear to be tightly bound to the potential model (with sharp resonances dominating the outcome of the collision process), the only general conclusion that can

* For the H-graphite surface oscillator the vibrational wavenumber $\bar{\nu} = \omega_0/2\pi c$ turns out to be 1807 and 2252 cm^{-1} for the adiabatic and diabatic cases, respectively.

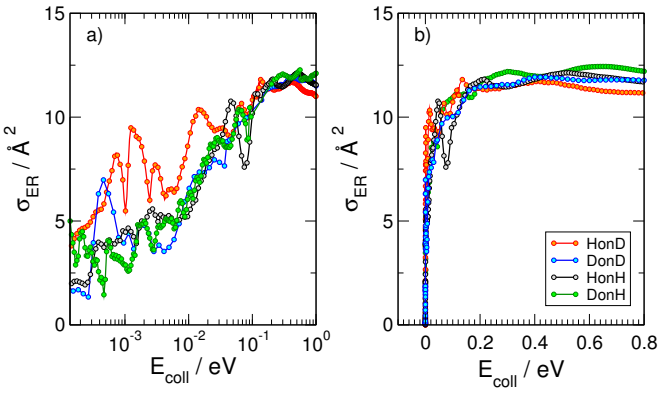

Fig. 3 Quantum ER cross sections for the four considered reactions as functions of collision energy, obtained with the adiabatic model. Logarithmic and linear scale for panels (a) and (b), respectively.

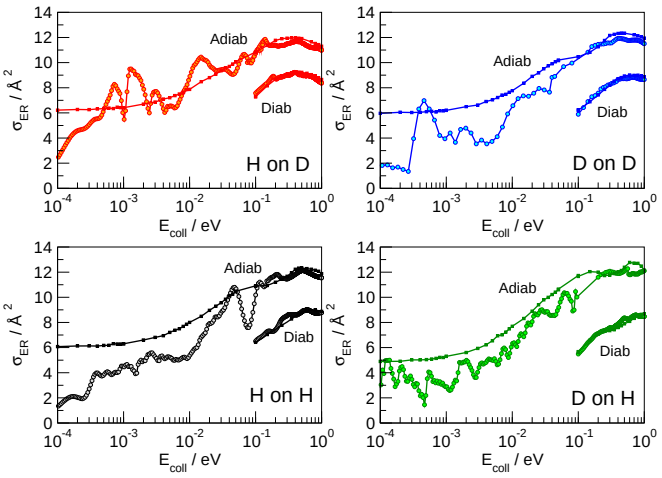

Fig. 4 Comparison between quantum (circles) and *quasi*-classical results (squares). The size of the squares matches the estimated uncertainties in QCT results.

be drawn for this energy range is that the collinear reaction probability is again highly affected by the mass of the incident and of target atom.

4.2 3D calculations

When the third spatial coordinate is added, the reactive cross sections for the Eley-Rideal H_2 recombination σ_{ER} can be computed, as well as the cross sections for non-reactive collisions giving rise to hot-atom species σ_{HA}. In Fig. 3, σ_{ER} computed with the adiabatic model is plotted as a function of the collision energy, for the four possible isotope combinations. The general behavior of such cross-sections was already extensively discussed in previous works [11,17–19]. At low energies, σ_{ER} decreases as the collision energy decreases, likely because of the strong, short-range interaction potential between the two atoms that prevents low energy projectiles to enter the exit channel if their de Broglie wavelength is larger than the range of the potential. Thus, the cross sections decay to zero for $E_{coll} \rightarrow 0$, though non-monotonically because of the presence of a number of sharp resonances. At moderate-to-high energy range, σ_{ER} reaches large values ($\sim$12 Å^2) in all the considered cases, much larger than those observed on many metal surfaces [10], where σ_{ER} barely reaches 1 Å^{2*}. This feature is rather peculiar of the graphitic substrate where, in contrast to many metals, target hydrogen atoms are found at a larger height above the surface and projectile atoms experience a reduced interaction *with the surface*. At even higher energies ($E_{coll} > 0.2$ eV), quantum oscillations appear in the cross section, as a consequence of the particular reaction mechanism that - by featuring a rapidly decreasing internal excitation of the product for increasing energies - allows the low-lying product vibrational levels to be selectively populated [17,18,27].

Importantly, a rather striking feature of the results shown in Fig. 3 is the disappearance of the isotopic effect observed in the collinear case, in agreement with the findings of previous quantum studies at high collision energies on a crude model PES [39]. This suggests that the dynamics is not as direct as the constrained collinear geometry forces it to be, and the reaction mechanism involves some energy "randomization" prior to reaction which hides the effect of the different mass combinations. No real "tendency" can be discerned in the quantum results, and the effect of an unfavorable mass-ratio must be offset by some non-collinear dynamical effects. Such effects though must be of classical nature, since *quasi*-classical trajectory calculations reproduce quantum results very well over a large energy range, and do not show isotope effects either. This is shown in Fig. 4, where the QCT cross-sections, reported alongside with the quantum results, differ considerably from the latter only in the very low energy region, and are shown to reproduce rather well (on average) the quantum results. Notice, though, that differently from the quantum results, the limiting classical cross-section at zero energy does not vanish, as expected for a barrierless classical reaction dynamics. For completeness, Fig. 4 also shows the results for the diabatic dynamical model (for clarity, only in the energy range where they are more reliable), which present a behavior similar to those obtained in the adiabatic limit, except for an overall reduction of the cross-section which correlates with the reduced exothermicity of the diabatic model.

More information about the reaction dynamics can be obtained by looking at the rovibrational populations of the molecular product. Results for the average internal energy,

∗ Notice though that a spin-statistical factor of 1/4 applies on graphitic substrates but does not on metals. This is due to the fact that the spin of the chemisorbed H atom is *not* quenched on graphene(ite), see *e.g.* Ref. 47.

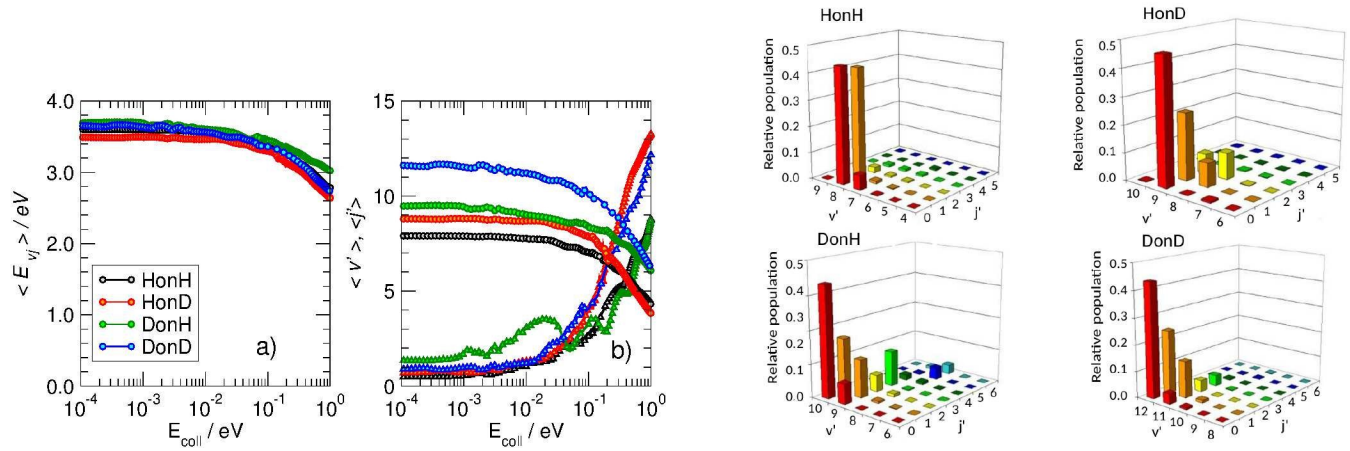

Fig. 5 Left: Average internal energy (panel a) and average quantum numbers (panel b) of the nascent molecules, as obtained in the adiabatic model. In (b) circles and triangles are for the averaged vibrational and rotational quantum numbers, respectively. Right: Distribution of the rovibrational states $(v'\, j')$ of the ER recombination products, computed at E_{coll} = 2 meV in the adiabatic case. Different panels refer to the four isotopic combinations considered.

and average vibrational and rotational quantum numbers are shown in Fig. 5 (left). As is evident from that figure, and in agreement with previous studies at high energies[11,17,18], the nascent molecules are internally hot, with *ca.* $3.0-3.5$ eV of the reaction exothermicity going in internal excitation of the Eley-Rideal product. In contrast to the behavior at high collision energies, though, internal excitation is mainly vibrational, the average rotational quantum number being rather small in the energy range $10^{-4}-10^{-1}$ eV *. This is not an artifact of the averaging procedure, since the detailed rovibrational distributions are rather peaked around few rovibrational states, as shown in Fig. 5 (right panel) at a representative energy of 2 meV. It is evident from that figure that the nascent molecule mostly appears in either one or two high-v, low$-j$ rovibrational states.

The behavior of the rotational excitation - which monotonically increases with the collision energy - correlates well with the reaction cross-sections, especially at high energies where the dynamics is classical. The rationale here is that, classically, the angular momentum j of the product molecule correlates well with the entrance orbital angular momentum l of the projectile-targon pair (*i.e.* $j \sim l$), as discussed previously[18], hence $< j >$ can be related to the reaction cross-section through the "maximum" impact parameter b_{max}, $l_{max} = b_{max}\mu v \approx \mu v\sqrt{\sigma_{ER}/\pi}$.

The above considerations suggest that in this realistic 3D case the reaction dynamics is determined by the relative motion in the entrance channel - similarly to what happens for the collinear approach -, but now the *orbital* angular motion of the colliding pair plays a primary role. If it were for the H-H potential only, "capture" of the projectile would not depend on the specific isotope combination, since the "capture radius" ρ_c reads as

$$\rho_c = \sqrt{\frac{n}{n-2}}\sqrt[n]{\frac{n}{2}-1}\sqrt[n]{\frac{\alpha}{E}}$$

when the long-range tail of the projectile-targon potential takes the form $U(r) = -\alpha/r^n$ $(n > 2)$. In the gas-phase, this result holds for arbitrarily small collision energies, and determines, *e.g.*, the Langevin capture rate constant that accurately describes low-temperature ion-molecule reactions ($n = 4$). It cannot strictly hold in our problem, though, since the projectile-targon attraction competes with the projectile-surface interaction (particularly in those large impact parameter trajectories which determine the size of the cross-section) and this competition strongly modifies the energy dependence of ρ_c. The surface *shields* the targon from low-energy projectiles and, conversely, *focuses* higher energy trajectories towards the target, thereby reducing (increasing) the capture radius at low (high) collision energies.

This is best seen in a simple model where the targon is held fixed at a height h ($h > 0$ when the target atom lies above the surface) and the surface is represented by a hard wall that has the simple effect of reverting the normal component of the projectile velocity, $v_z \to -v_z$ (see Fig. 6). In this model, the orbital angular momentum of the projectile undergoes a sudden change $l \to l'$ upon collision with the surface, namely

$$\Delta l^2 = l'^2 - l^2 = -4uhv_xv_z$$

if $\mathbf{r}_P = (u, -h)$ represents the projectile position in the scattering plane (referenced to the targon) at the time of the impact

* The "isotope effect" which is apparent in the average vibrational quantum numbers just reflects the different level spacing of the H_2, HD and D_2 molecules, see Fig. 5, panel (a)

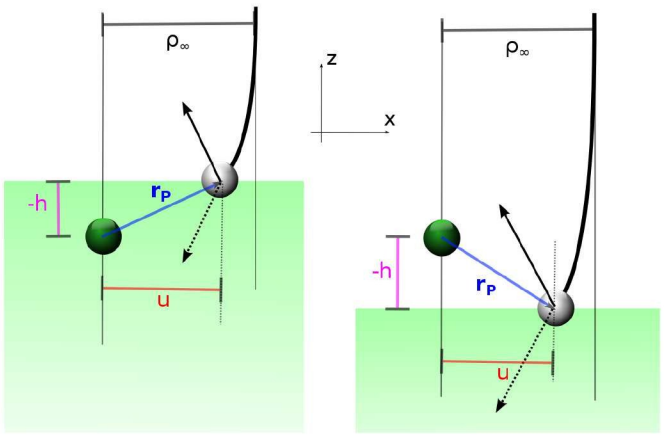

Fig. 6 Surface-mediated capture. The targon (green balls) is held fixed at height h above the surface ($h < 0$ in the left panel and $h > 0$ on the right) and collision of the projectile (grey balls) with the surface occurs at a position $\mathbf{r}_P = (u, -h)$ in the scattering plane. The arrows indicate the projectile speed before (dashed) and after (thin line) the bounce and ρ_∞ is the impact parameter of the trajectory.

and $\mathbf{v} = (v_x, v_z)$ its speed* (Fig. 6). Since for an attractive interaction $v_x v_z \geq 0$ (≤ 0) holds to the right (left) of the targon atom, the change Δl is *negative* for a targon *above* the surface and *positive* otherwise. As a consequence, the effective barrier ruling the capture process decreases (increases) when the target lies above (below) the surface and, correspondingly, the capture radius becomes larger (smaller) than its gas-phase value†.

Real surfaces are not hard walls and display a more intricate competition with the targon field of forces than the one outlined above. Nevertheless, for the large-impact parameter trajectories we are interested in, the picture above is mainly modified only to the extent that the height of the turning point becomes energy dependent, the smaller the collision energy is the higher the "altitude" where the projectiles reverts its motion. In particular, the location of the physisorption wall (relative to the chemisorpton well) determines the limiting "height of the targon" at vanishing collision energies. Its negative value considerably reduces the size of the gas-phase capture radius and makes it finite at zero energy.

Overall, even though this argument does not explain the precise form that σ_{ER} takes as a function of energy, it does suggest a reason why the reaction cross-section does *not* depend on the

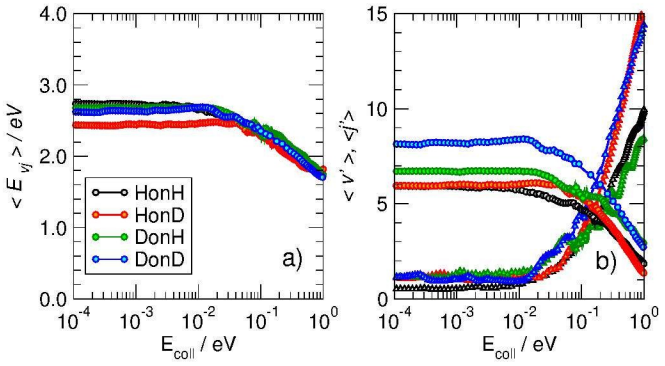

Fig. 7 Average internal energy (panel a) and average quantum numbers (panel b) of the nascent molecules, as obtained in the diabatic model. In (b) circles and triangles are for the averaged vibrational and rotational quantum numbers, respectively.

mass combination of the colliding pair: reaction is dominated by the capture process - *i.e.* collisions are mainly glancing rather than head-on - and this is only marginally affected by isotopic substitutions.

Fig. 7 shows the average internal energy, and the average vibrational and rotational quantum numbers of the product molecules, as obtained from the diabatic model, similarly to Fig. 5 for the adiabatic limit. As can be seen from this figure, the dynamics is very similar in the two models, the only difference being the smaller reaction exothermicity described in the diabatic limit, which determines a corresponding decrease of the internal energy of the products. In other words, the change in the reaction energetics does not affect the translation energy of the products, only its internal content. This highlights the importance of including energy relaxation to the surface into the reaction dynamics in order to accurately assess the internal excitation of the product molecule - the "missing energy" of the diabatic model is just a crude way to describe such energy transfer, energy is stored in the puckered carbon atom and released to the substrate upon molecular formation.

In contrast with the ER reaction, the cross section for the formation of hot-atom species is characterized by a strong isotopic effect. This is shown in Fig. 8, which reports σ_{HA} as a function of the energy of the incident atom for the four isotope combinations. As evident from the figure, when the incident atom is hydrogen (black and red curves), σ_{HA} barely reaches 2 Å^2, whereas when the incident atom is deuterium (green and blue curves), the cross section significantly increases and can be as large as ~ 16 Å^2. In our dynamical model, the HA formation corresponds to the situation in which the reactive event ends with a large momentum along ρ and with the incident atom bound (normal to the surface) in the physisorption well. Hence, the larger deuterium cross sections are simply a consequence of the larger number of final physisorbed bound states available to the incident atom. The well is in fact only

* If needed, v_x and v_z can be expressed in terms of $\mathbf{r}_P$ and the constants of motion in the targon field, namely as $v_x = (-v_r u + v_\omega h)/r_P$ and $v_z = (v_r h + u v_z)/r_P$ where $v_r = \sqrt{2(E - l^2/2mr^2 - U(r))/m}$ and $v_\omega = -l/mr_P v_\omega$ ($U(r)$ being the projectile-targon spherical potential).

† The case $h = 0$ with the targon "in the plane" of the surface does not modify l, hence in this case the rotational angular momentum of the product molecules exactly matches the angular momentum of the reagents. This is the conservation of the angular momentum alluded to above.

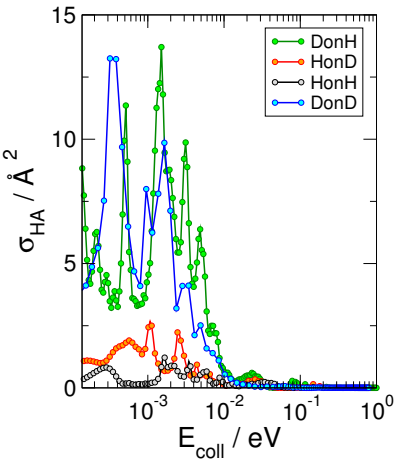

Fig. 8 Quantum cross sections for the "hot-atom" formation for the four considered isotopic combinations as a function of collision energy, computed within the adiabatic model.

$\sim$7.75 meV in our model potential and supports only one state for H and two for D, but similar results are expected for a more realistic physisorption well depth[22,23]. In any case, and irrespective of the mass combination, σ_{HA} quickly vanishes for $E_{coll} \gtrsim 10^{-2}$ eV, when projetile energy becomes too large for trapping in the physisorption well.

A word of caution is appropriate here. Our dynamical model is not entirely adequate to simulate hot-atom formation, since within the flat surface approximation a free motion along ρ implies that *both* incidon and targon might be moving along the direction parallel to the surface. This situation should *not* be allowed in our case where the target atom is held in place by a strong, directional bond with the surface. The model though does capture the main effects of the presence of the target atom - *i.e.* the increase of surface corrugation and energy accommodation -, hence we are confident that it correctly describes the "initial" trapping cross section. After this step it is the dynamical response of the C-H bond that determines whether the trapped incidon species interacts again with the targon or is left free to move on the surface. In this respect, our results can be considered the limiting case where the targon rebounce (a CH bending) is slow enough to not affect the projectile atom after the first collision.

5 Summary and Conclusions

In this work we have used quantum dynamics to investigate isotope effects in collision induced processes involving hydrogen/deuterium atoms on graphite at the cold collision energies typical of the ISM. We focused on chemisorbed target atoms and analyzed Eley-Rideal reaction and trapping dynamics for the four possible isotopic combinations, using a time-dependent "two-wavepacket" method and *quasi*-classical dynamics.

Our simulations show that ER hydrogen formation is affected by isotopic substitution only in the collinear approach. In this case, the P_{ER} curves for different mass combinations result from an intricate interplay of kinematic and quantum effects but, at high energies, are well rationalized by a simple *quasi*-classical impulsive model of the dynamics. In the 3D case, on the other hand, this marked isotopic effect disappears and the four considered reactions show almost identical trends and values for σ_{ER}, likely as a consequence of the fact that "capture" of the projectile does not depend on the specific mass combination. This suggests two different "mechanisms" for product formation, namely through either "head-on" or "glancing" collisions. The first presents a marked isotopic effect but has a limited weight in the cross-section while the second has the largest weight but is less sensitive to mass effects.

In contrast to Eley-Rideal reaction, the mass of the projectile does strongly influence hot-atoms formation. σ_{HA} reaches considerably large values ($\sim$ 16 Å^2) when the atom from the gas phase is the heaviest, and barely attains 2 Å^2 for hydrogen. This is a direct consequence of the increased number of bound states in the physisorption well that can host the trapped incidon. This effect, likely occurring on different surfaces as well (*e.g.* those covered by ice mantles), might be responsible for some deuterium enrichment in the ISM grains, with impact on deuterium fractionation* through surface reactions. It is worth noticing though that such fractionation is mainly a gas-phase effect related to the efficient 'primary' fractionation in H_3^+ ($[H_2D^+]/[H_3^+] \sim 10^4 [HD]/[H_2]$), and the primary role of surfaces is through accretion, which deplets H_2D^+-destroying molecules (notably CO) and makes formation of higher deuterated species D_2H^+ and D_3^+ possible[48,49].

Comparison of the results obtained in the adiabatic and in the diabatic limits suggests that the reaction is only marginally affected by the lattice dynamics - *ab initio* molecular dynamics simulations including the lattice dynamics indeed found cross-section values intermediate between these two limits[21] - but for a correct description of the internal excitation of the product molecules it is essential to include energy transfer to the carbon atom holding the targon in place. Work is currently in progress to lift this static surface approximation and describe the dynamical role that the substrate carbon atoms (and the ensuing energy dissipation to the surface) plays in the reaction.

* That is, the observation of deutereted molecules well in excess (up to 10^{11}) the statistical predictions based on the cosmic D/H ratio $\sim 10^{-5}$.

6 Acknowledgments

This work has been supported by Regione Lombardia and the CINECA High Performance Computing Center through a LISA Initiative (2014) grant.

References

1 V. Wakelam, I. Smith, E. Herbst, J. Troe, W. Geppert, H. Linnartz, K. Öberg, E. Roueff, M. Agúndez, P. Pernot, et al., Space Sci. Rev. **156**, 13 (2010).
2 R. J. Gould and E. E. Salpeter, Astrophys. J. **138**, 393 (1963).
3 D. Hollenbach and E. E. Salpeter, J. Chem. Phys. **53**, 79 (1970).
4 D. Hollenbach and E. E. Salpeter, Astrophys. J. **163**, 155 (1971).
5 B. T. Draine, Annu. Rev. Astron. Astrophys. **41**, 241 (2003).
6 P. Parneix and P. Brechignac, A&A **334**, 363 (1998).
7 A. J. Farebrother, A. J. Meijer, D. C. Clary, and A. J. Fisher, Chem. Phys. Lett. **319**, 303 (2000).
8 A. J. H. M. Meijer, A. J. Farebrother, D. C. Clary, and A. J. Fisher, J. Phys. Chem. A **105**, 2173 (2001).
9 M. Rutigliano, M. Cacciatore, and G. D. Billing, Chem. Phys. Lett. **340**, 13 (2001).
10 B. Jackson and D. Lemoine, J. Chem. Phys. **114**, 474 (2001).
11 X. Sha, B. Jackson, and D. Lemoine, J. Chem. Phys. **116**, 7158 (2002).
12 S. Morisset, F. Aguillon, M. Sizun, and V. Sidis, Phys. Chem. Chem. Phys. **5**, 506 (2003).
13 S. Morisset, F. Aguillon, M. Sizun, and V. Sidis, J. Phys. Chem. A **108**, 8571 (2004).
14 D. Bachellerie, M. Sizun, D. Teillet-Billy, N. Rougeau, and V. Sidis, Chem. Phys. Lett. **448**, 223 (2007).
15 D. Bachellerie, M. Sizun, F. Aguillon, D. Teillet-Billy, N. Rougeau, and V. Sidis, Phys. Chem. Chem. Phys. **11**, 2715 (2009).
16 M. Sizun, D. Bachellerie, F. Aguillon, and V. Sidis, Chem. Phys. Lett. **498**, 32 (2010).
17 R. Martinazzo and G. F. Tantardini, J. Phys. Chem. A **109**, 9379 (2005).
18 R. Martinazzo and G. F. Tantardini, J. Chem. Phys. **124**, 124702 (pages 14) (2006).
19 S. Casolo, R. Martinazzo, M. Bonfanti, and G. F. Tantardini, J. Phys. Chem. A **113**, 14545 (2009).
20 M. Bonfanti, S. Casolo, G. F. Tantardini, and R. Martinazzo, Phys. Chem. Chem. Phys. **13**, 16680 (2011).
21 S. Casolo, G. F. Tantardini, and R. Martinazzo, Proc. Natl. Acad. Sci. U. S. A. **110**, 6674 (2013).
22 E. Ghio, L. Mattera, C. Salvo, F. Tommasini, and U. Valbusa, J. Chem. Phys. **73**, 556 (1980).
23 M. Bonfanti, R. Martinazzo, G. F. Tantardini, and A. Ponti, J. Phys. Chem. C **111**, 5825 (2007).
24 B. Lepetit and B. Jackson, Phys. Rev. Lett. **107**, 236102 (2011).
25 S. Morisset, F. Aguillon, M. Sizun, and V. Sidis, J. Chem. Phys. **122**, 194702 (pages 8) (2005).
26 D. Bachellerie, M. Sizun, F. Aguillon, and V. Sidis, J. Phys. Chem. A **113**, 108 (2009).
27 R. Martinazzo and G. F. Tantardini, J. Chem. Phys. **124**, 124703 (pages 7) (2006).
28 T. Zecho, A. Güttler, X. Sha, B. Jackson, and J. Küppers, J. Chem. Phys. **117**, 8486 (2002).
29 A. Güttler, T. Zecho, and J. Küppers, Chem. Phys. Lett. **395**, 171 (2004).
30 T. Zecho, A. Güttler, and J. Küppers, Carbon **42**, 609 (2004).
31 L. Jeloaica and V. Sidis, Chem. Phys. Lett. **300**, 157 (1999).
32 X. Sha and B. Jackson, Surf. Sci. **496**, 318 (2002).
33 E. Aréou, G. Cartry, J.-M. Layet, and T. Angot, J. Chem. Phys. **134**, 014701 (2011).
34 M. Bonfanti, B. Jackson, K. H. Hughes, I. Burghardt, and R. Martinazzo, J. Chem. Phys. **143**, 124703 (2015).
35 M. Bonfanti, B. Jackson, K. H. Hughes, I. Burghardt, and R. Martinazzo, J. Chem. Phys. **143**, 124704 (2015).
36 A. Güttler, T. Zecho, and J. Küppers, Carbon **42**, 337 (2004).
37 F. Islam, E. R. Latimer, and S. D. Price, J. Chem. Phys. **127**, 064701 (2007).
38 E. R. Latimer, F. Islam, and S. D. Price, Chem. Phys. Lett. **455**, 174 (2008).
39 A. J. H. M. Meijer, A. J. Farebrother, and D. C. Clary, J. Phys. Chem. A **106**, 8996 (2002).
40 M. Rutigliano and M. Cacciatore, ChemPhysChem **9**, 171 (2008).
41 M. Persson and B. Jackson, J. Chem. Phys. **102**, 1078 (1995).
42 D. Lemoine and B. Jackson, Comput. Phys. Commun. **137**, 415 (2001).
43 R. Martinazzo and G. F. Tantardini, J. Chem. Phys. **122**, 094109 (pages 9) (2005).
44 D. Lemoine, J. Chem. Phys. **101**, 3936 (1994).
45 M. Feit, J. Fleck, and A. Steiger, J. Comput. Phys. **47**, 412 (1982).
46 D. E. Manolopoulos, J. Chem. Phys. **117**, 9552 (2002).
47 S. Casolo, O. M. Lovvik, R. Martinazzo, and G. F. Tantar-

dini, J. Chem. Phys. **130**, 054704 (2009).
48 T. Millar, Planetary and Space Science **50**, 1189 (2002), ISSN 0032-0633, special issue on Deuterium in the Universe.
49 T. J. Millar, Astronomy & Geophysics **46**, 2.29 (2005).